ACS SENSORS

pubs.acs.org/acssensors Article

Skin-Conformal Sandwich-Structured SERS Superlattice Platform for Non-Invasive Depression Detection

Hangzhe Shao,[#] Shuangshuang Wu,[#*] Lingli Zhang, Bohang Ye, Qiaoyun Luo, Kanzhen Tong, Liping Song,[*] and Youju Huang[*]

Cite This: *ACS Sens.* 2026, 11, 2763−2773 Read Online

ACCESS | Metrics & More | Article Recommendations | Supporting Information

ABSTRACT: Flexible wearable biochemical sensors hold great promise for personalized health monitoring. However, achieving ultrahigh molecular sensitivity, conformal skin adhesion, and efficient sweat handling within a single device remains a critical challenge. Here, we present a fully integrated wearable sweat-sensing platform that seamlessly combines a biocompatible adhesive hydrogel, an ultrasensitive sandwich-structured surface-enhanced Raman scattering (SERS) architecture, and microfluidic sweat-collection channels for non-invasive monitoring of dopamine, a key biomarker associated with depression. The central component of the system is a dual-layer heterogeneous superstructure. Specifically, a highly ordered Au nanoparticle (Au NP) superlattice forms the bottom layer, offering uniform and dense plasmonic hotspots, while the top layer is based on double-shelled hollow Au@Au−Ag nanocages functionalized with Raman reporters and aptamer sequences. Furthermore, DNA-guided hybridization forms a robust "nanolock" junction that ensures strong interparticle coupling and provides excellent specificity. This configuration yields an exceptional SERS enhancement factor of 1.57×10^{11}, enabling nanomole-level dopamine detection (limit of detection: 3.78×10^{-14} M) with excellent reproducibility (RSD = 9.02%) and high chemical specificity. To adapt the sensing unit for on-body use, the SERS chip is embedded within an adhesive, deformable, and biocompatible polyethylene glycol hydrogel. Featuring engineered microfluidic channels, this hydrogel autonomously transports sweat to the sensing area, thereby guaranteeing precise detection alongside consistent conformal contact and comfort. This multifunctional, integrated platform has the potential to overcome longstanding limitations in sensitivity, stability, biocompatibility, and sweat management that hinder conventional wearable sensors. It provides a powerful route toward a versatile design framework for next-generation wearable bioelectronics.

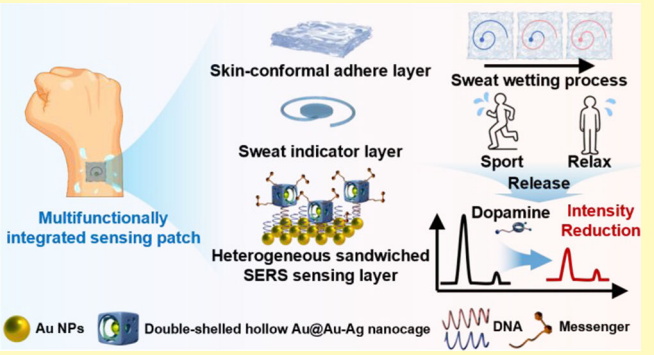

KEYWORDS: *wearable biochemical sensors, multifunctional integration, heterogeneous sandwich structure, flexible hydrogel interface, mental-health detecting*

Flexible wearable biosensors are ushering in a new paradigm of healthcare by enabling continuous and non-invasive acquisition of biochemical information.[1−3] Among all biofluids, sweat stands out as an especially appealing substrate for biochemical sensing. Because its endogenously secreted metabolites can be accessed without invasive sampling, which offers an inherently user-friendly and non-disruptive diagnostic approach. This capability is particularly crucial for mental disorders such as depression.[4] Alleviating patient stress, eliminating sampling-induced artifacts, and enabling frequent, real-world assessments are indispensable for achieving precise and clinically meaningful monitoring. Recently, research has clearly demonstrated that depression is accompanied by significant alterations in the levels of key neurotransmitters (such as dopamine, serotonin, cortisol, norepinephrine) and neuropeptides, providing a potential basis for objective diagnosis.[5,6] Taking dopamine, which exists in trace amounts in bodily fluids, as an example: its concentration in human blood is below 5×10^{-3} M, and in human sweat, it is even lower than 2.5×10^{-6} M.[7−9] This demands detection technologies with extremely high sensitivity and stability. More complexly, to realize daily, objective monitoring of depression and other psychiatric conditions, wearable sweat sensors must combine strong and conformal adhesion to skin, ultrahigh molecular sensitivity capable of detecting trace

Received: December 14, 2025
Revised: February 12, 2026
Accepted: March 4, 2026
Published: March 10, 2026

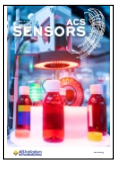

https://doi.org/10.1021/acssensors.5c04789
ACS Sens. 2026, 11, 2763−2773

Scheme 1. Overview of the Multifunctionally Integrated Wearable Sweat Sensing System[a]

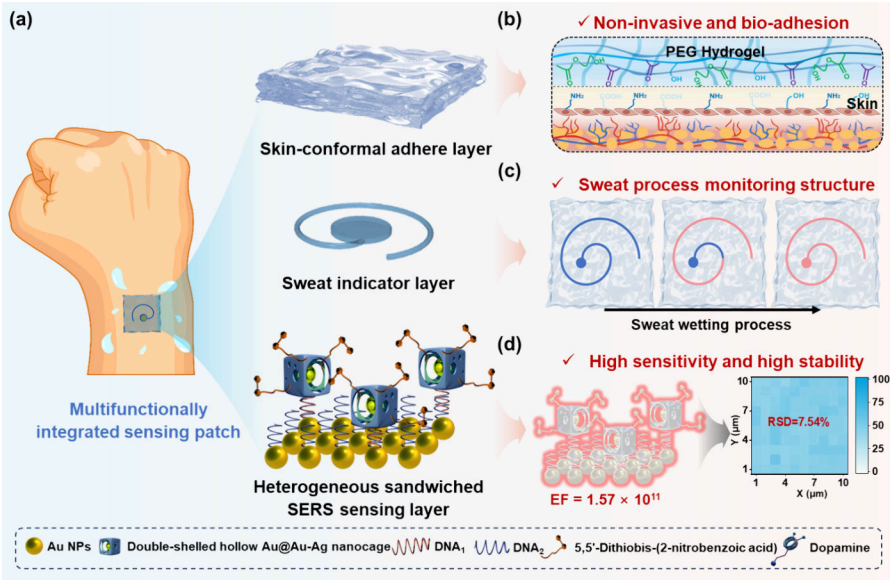

[a](a) Structural composition of the device, consisting of a skin-adhesive hydrogel interface, microfluidic channels for sweat guidance and visual indication, and a sandwich-structured SERS sensing module composed of ordered Au NPs and double-shelled Au@Au−Ag nanocages. (b) Non-invasive and biocompatible adhesion of the PEG-based hydrogel that conforms to skin topography and minimizes motion-induced artifacts. (c) Visual indication of the water-wetting and sweat transport process in the hydrogel microchannel, enabling intuitive observation of fluid progression. (d) High sensitivity and high stability of SERS signals from the sandwich structure.

neurotransmitters, and efficient management of small volumes of sweat, which all within a single integrated platform.[10−12]

On the one hand, wearable sweat sensors need a skin-compatible and adhesive interface that maintains intimate contact with the dynamically moving epidermis to reduce signal drift.[13−15] Conventional polymer substrates such as polyimide (PI) or polyethylene terephthalate (PET) exhibit mechanical properties that do not match those of human skin, resulting in interfacial slippage and signal drift during motion.[16−18] In addition, sweat may also accumulate at the interface, causing irritation and interfering with sensing accuracy.[19,20] Moreover, the inherently low secretion rate and rapid evaporation of sweat make stable sampling difficult. Hydrogels offer an effective solution to these limitations: their tissue-like softness, excellent wettability, and intrinsic adhesion to skin enable stable, long-term contact, while their hydrophilic networks promote rapid absorption and transport of micro-volume sweat.[21] These features make hydrogels highly promising as an interface material for reliable and comfortable wearable sweat sensing.

On the other hand, to enable quantitative sweat analysis, various detection strategies, including electrochemical sensing, colorimetry, piezoelectric sensing, impedance analysis, and surface-enhanced Raman scattering (SERS), have been extensively explored.[22−25] Among them, plasmonic superstructures offer unique advantages. Their precisely engineered nanoscale architectures enable strong and uniform local electromagnetic enhancement, dramatically boosting optical signal intensity and providing the physical basis required for detecting ultralow-abundance neurotransmitters.[26,27] However, achieving high sensitivity while maintaining structural and signal stability under wearable conditions remains a significant challenge.[28] The need to balance robust plasmonic enhancement with reliable performance continues to limit the practical application of existing SERS substrates in flexible biochemical sensing systems.

In response to these challenges, we designed a multifunctional and integrated wearable sweat-sensing system that combines a biocompatible hydrogel interface, a highly sensitive sandwich-structured SERS module, and a microfluidic sweat-collection network within a single platform (Scheme 1). A self-adhesive polyethylene glycol (PEG) hydrogel serves as a soft, transparent, and stretchable substrate that conforms to natural skin deformation, which ensures stable optical pathways and mechanical reliability during long-term wear (Scheme 1b). Its hydrophilic polymer network supports rapid sweat uptake and provides a benign environment suitable for physiological interfaces. The sensing core adopts a heterogeneous Au-based sandwich architecture that consists of a bottom Au NPs superlattice with long-range order and uniform spacing and a top layer of double-shelled hollow Au@Au−Ag nanocages functionalized with Raman reporters. Furthermore, DNA-guided hybridization assembles the two layers into a defined nanogap configuration that produces a dense array of reproducible plasmonic hotspots. This hierarchical structure overcomes the stochastic nature of conventional SERS substrates and provides strong electromagnetic enhancement with high signal stability (Scheme 1d). Microfluidic channels embedded within the hydrogel autonomously guide sweat from the skin into the sensing region and enable efficient delivery of trace biomarkers (Scheme 1c). Through this integrated design, the wearable sensor achieves picomolar-level dopamine detection with excellent reproducibility, strong anti-interference behavior, and stable on-body performance (Scheme 1a). The system demonstrates the feasibility of real-time and non-invasive monitoring of depression-associated biochemical markers and offers a promising technological path toward objective mental health assessment and personalized therapeutic management.

https://doi.org/10.1021/acssensors.5c04789
ACS Sens. 2026, 11, 2763−2773

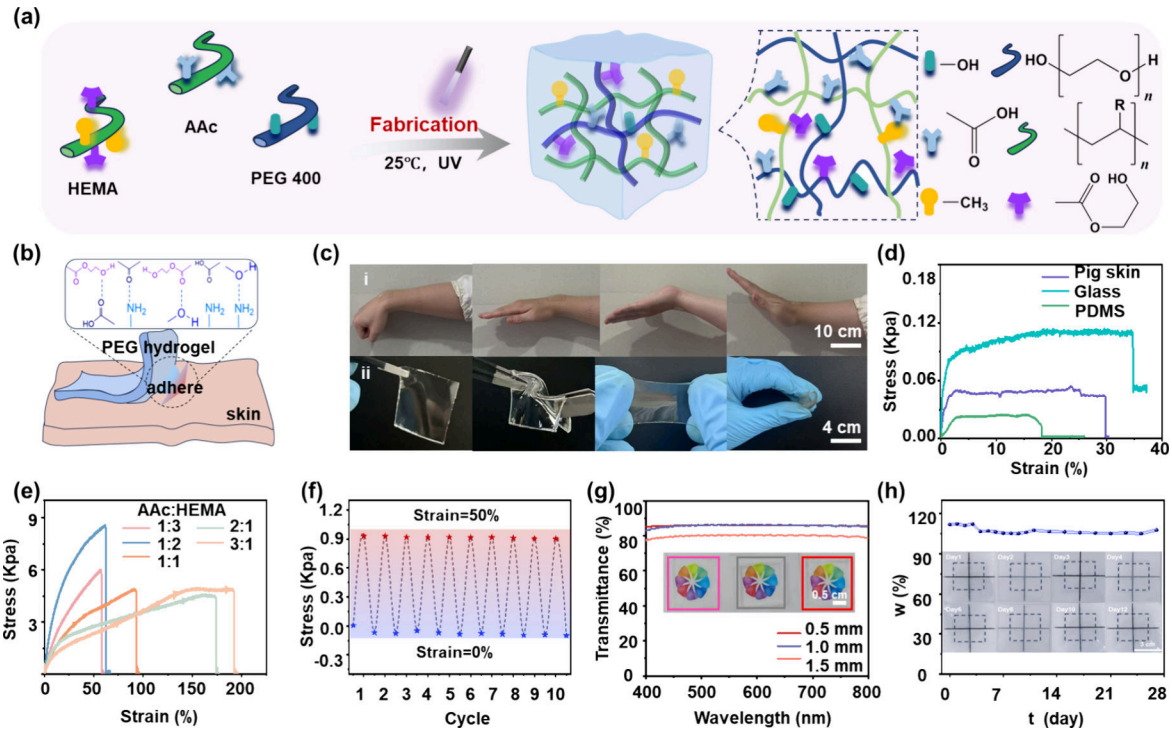

Figure 1. Design and performance of a hydrogel patch. (a) Schematic of synthesis of the hydrogel patch. (b) Schematic illustration of the conformal adhesion between a functional hydrogel and human skin. (c) Macro-scale depiction of common activities and mechanical deformations of the hydrogel patch adhered to skin. (d) Adhesion strength curve on various substrate surfaces. (e) Tensile stress-strain curves of the hydrogel patch. (f) Tensile stress-strain cycling curves of the hydrogel patch. (g) Light transmittance properties and macroscopic appearance of hydrogels with varying thicknesses. (h) Long-term stability data.

RESULTS AND DISCUSSION

Design and Performance of the Hydrogel Patch

To achieve highly transparent, arbitrarily deformable, self-adhesive, and biocompatible performance of patch, a PEG hydrogel patch with hydrophilic polymer network was utilized as the optical sensing substrate. Accordingly, the hydrogel patch was prepared by free radical copolymerization of hydroxyethyl methacrylate (HEMA), acrylic acid (AAc), and 2-hydroxy-2-methylpropiophenone (photo initiator) in PEG-400 under ultraviolet (UV) irradiation (Figure 1a).[29] The strong and conformal adhesion of the hydrogel patch to human skin originates from synergistic intermolecular interactions (Figure 1b). Specifically, the −OH and −COOH groups in the hydrogel form multiple hydrogen bonds with polar functional groups (e.g., −OH and $-NH_2$) present on the stratum corneum and skin surface proteins. In addition, under near-neutral skin pH conditions, partial deprotonation of −COOH groups to $-COO^-$ enables favorable electrostatic interactions with positively charged amino groups ($-NH_3^+$) in keratin, collectively ensuring robust adhesion under skin deformation.[30,31] This strong adhesion allows it to stay firmly on the skin without peeling off, even when twisted or stretched in any direction (Figure 1c-i). Consequently, this mechanism translated into reliable adhesion across diverse materials, from biological tissues like porcine skin to synthetic surfaces like glass and silicone polymers (Figure 1d). The copolymerization of AAc and HEMA resulted in a densely cross-linked three-dimensional network, which provided abundant energy dissipation sites and thereby enhanced the mechanical properties of the hydrogel. To elucidate the correlation between composition and mechanical performance, tensile tests were conducted on hydrogels with varying compositions. As the AAc content increased, the tensile strain of the hydrogel increased from 91 to 191%, while raising the HEMA content enhanced the tensile strength to 8.6 kPa (Figure 1e). Owing to its superior mechanical properties, the AAc-50% hydrogel was selected for subsequent investigations. Furthermore, the hydrogel demonstrated satisfactory cyclic stretchability, confirming its durability under 10 times repeated deformation (Figure 1f). Moreover, the hydrogel tolerated complex deformations (including folding, bending, and twisting) and demonstrated significant flexibility (Figure 1c-ii). The hydrogel patch remained highly transparent across the range of thicknesses tested, making it highly suitable for use in optical sensors (Figures 1g and S1). As the inset shows, the seven-color flower pattern beneath could be easily seen through the hydrogel. Not only that, but the hydrogel also demonstrated remarkable dehydration resistance in an open environment, retaining 106% of its original mass over 28 days (Figure 1h). The initial slight mass increase is attributed to the hygroscopic nature of PEG-400, which enables minor moisture absorption upon initial exposure.

Owing to the critical importance of biocompatibility for wearable applications, an assessment of the hydrogel's cytocompatibility was conducted with L-929 cells. The material demonstrated excellent biocompatibility, and cell viability retained a high level (approximately 96%) even at high extract concentrations (up to 20 mg/mL) (Figure S2a). This dose-independent response strongly suggested a favorable interaction with biological environments. Furthermore, confocal fluorescence microscopy images

https://doi.org/10.1021/acssensors.5c04789
ACS Sens. 2026, 11, 2763−2773

revealed robust cellular adherence and a predominantly viable cell population, with minimal apoptotic activity observed (Figure S2b). These findings collectively demonstrated the outstanding biosafety profile of the hydrogel patch, thereby establishing its potential for prolonged skin contact and biomedical applications. To further assess skin compatibility under practical use conditions, on-skin wear studies were conducted on healthy adult volunteers (Figures S3 and S4). The hydrogel patches were applied to the dorsal hand for short-term wearing sessions, during which stable adhesion and conformal contact were maintained. Upon removal, no visible signs of erythema, edema, papules, or other irritation were observed compared to adjacent untreated skin. Moreover, no delayed skin reactions were detected within 24 hours after removal. These results demonstrate that the hydrogel-based sensor interface exhibits good skin tolerance and does not cause noticeable skin sensitivity under the tested conditions, supporting its suitability for wearable applications.

Design of the Highly Sensitive and Stable SERS Substrate

The primary sensing principle of our integrated wearable sensor depends on the orderly arranged Au NPs. As shown in Figure S5, the highly monodisperse and uniformly sized Au NPs (15.4 ± 3.2 nm) were employed to fabricate superlattice film following the previously established approach.[29] Accordingly, a large-area (∼7 cm^2), uniform, dense monolayer hexagonal close-packed (HCP) Au NPs superlattice film was produced via ligand-induced interfacial assembly by employing oleyl amine as a dynamic complexing agent (Figure 2a). To validate the enhancement of SERS performance by the ordered structure of Au NPs superlattice film, a disordered Au NPs film was prepared as a control.[32] In the UV−vis spectra, strong plasmonic coupling between the Au NPs in the superlattice resulted in a narrower and more redshifted absorption peak compared to those of both disordered films and solutions (Figure 2b). TEM investigation provided clear visual confirmation, showing that the small, isolated "superlattice domains" in the disordered film resulted in variations in the spacing between the Au NPs (Figures 2c and S6). In contrast, the superlattice film exhibited a closely-packed and ordered arrangement with uniform spacing (3.26 ± 1.33 nm) between the Au NPs (Figure 2d,e). The long-range ordered and closely-packed arrangement of the Au NPs superlattice film ensures the ordered and uniform distribution of Raman hot spots, resulting in remarkable SERS performance and highly stable detection capabilities. On this basis, the arrangement of Au NPs in the different film were quantitatively analyzed using Voronoi tessellation, where each Au NP as a seed and its boundaries forming where regions meet. The Au NPs nanofilm often involve stacking layers with lattice mismatches. The Au NPs superlattice film exhibited regular hexagonal boundaries and a uniform area distribution (194 ± 70 nm^2), whereas the disordered Au NPs film displayed varied stacking arrangements and a differentiated area distribution (232 ± 101 nm^2) due to its lattice mismatch (Figures 2f,g and S7). Meanwhile, finite-difference time-domain (FDTD) simulation predictions attributed the formation of intensely enhanced and uniform hot spots in the ordered Au NPs superlattice film to its closely-packed, periodic nanostructure (Figure 2h). This paves the way for its use as a highly stable SERS substrate. In a comparative SERS study using 4-mercaptobenzoic acid (4-MBA) as the probe molecule under 785 nm laser excitation. The Au NPs superlattice film significantly outperformed the disordered monolayer film, exhibiting a remarkable 5-fold enhancement in signal strength at the characteristic 1075 cm^{-1} Raman peak, which is attributed to the symmetric stretching vibration mode of the benzene ring skeleton in the 4-MBA molecule.[33]

Furthermore, the superlattice structure demonstrated excellent signal reproducibility and operational stability across a series of 100 measurements, with a low relative standard deviation (RSD) of 7.54% attesting to its reliability. (Figure 2i−k).[34] This enhanced performance can be attributed to the uniform hot-spot distribution and strong inter-particle plasmonic coupling within the highly ordered superlattice architecture, which collectively enhances electromagnetic field consistency and intensity. The results highlight the crucial role of nanoscale organization in optimizing SERS substrates for sensitive and reliable detection.

Multilayered plasmonic nanostructures, featuring intraparticle nanogaps, greatly amplify electromagnetic fields and produce intense hotspots by leveraging collective excitation and multimode plasmon coupling. To create a substrate for highly sensitive and localized Raman signals, double-walled hollow nanoparticle superstructures with distinct gaps and porous nano-shells were synthesized via a continuous galvanic replacement reaction (GRR).[35] The synthetic procedure commenced with Au NPs (10.2 ± 0.8 nm), which served as the core (Figures 3a and S8). Subsequent epitaxial deposition of Ag was achieved through the reduction of Ag^+, mediated by ascorbic acid (AA), which resulted in Au@Ag nanocubes with an average edge length of 18.9 ± 2.2 nm (Figure S9). The deposition of Ag was accompanied by a blue shift in the absorption peak from 520 to 430 nm, which aligns with the intrinsic surface plasmon resonance peak of Ag NPs (Figure S9c). Then, the as-prepared Au@Ag nanocubes were utilized as sacrificial templates for the preparation of hollow superstructures with well-defined interior gaps and porous features via a halide-ion-induced GRR. This process is based on the principle of GRR: metal ions with a high reduction potential can oxidize metals with a lower reduction potential, leading to their own reduction and deposition as metallic atoms. Owing to the high standard reduction potential of the $AuCl_4^-$/Au pair (0.93 V), Au^{3+} ions are able to oxidize metallic Ag to form AgCl.

$$3Ag(s) + AuCl_4^-(aq) \rightarrow Au(s) + 3AgCl(s) + Cl^-(aq) \quad (1)$$

The resulting AgCl subsequently participates in the reaction, and along with additional Ag from the etchant, co-deposits onto the nanoparticle surface. Through this intricate process, monoshell hollow Au@Au−Ag nanocages were ultimately formed (Figures 3b and S10). The resulting Au@Au−Ag nanocages exhibited a slightly increased edge length of 23.5 ± 3.8 nm, with a shell thickness of approximately 6.2 ± 0.9 nm. It is crucial to emphasize that employing a relatively high concentration of cetyltrimethylammonium chloride (CTAC) was essential. It functioned as a surfactant to prevent aggregation while simultaneously supplying chloride ions to initiate etching from the side facets. This process was pivotal in forming the porous shell structure, which was critical for ensuring an increased density of Raman hot spots. Through iterative silver deposition and subsequent GRR conducted for precisely controlled durations, double-shelled hollow Au@Au−Ag nanocages with uniform morphology (33.4 ± 6.5 nm) and well-defined gaps (10.8 ± 2.6 nm) were constructed (Figures 3c and S11,S12). Further characterization by high-angle annular dark-field scanning transmission electron microscopy (HAADF-STEM) and energy-dispersive X-ray spectroscopy (EDS) mapping confirmed

https://doi.org/10.1021/acssensors.5c04789
ACS Sens. 2026, 11, 2763−2773

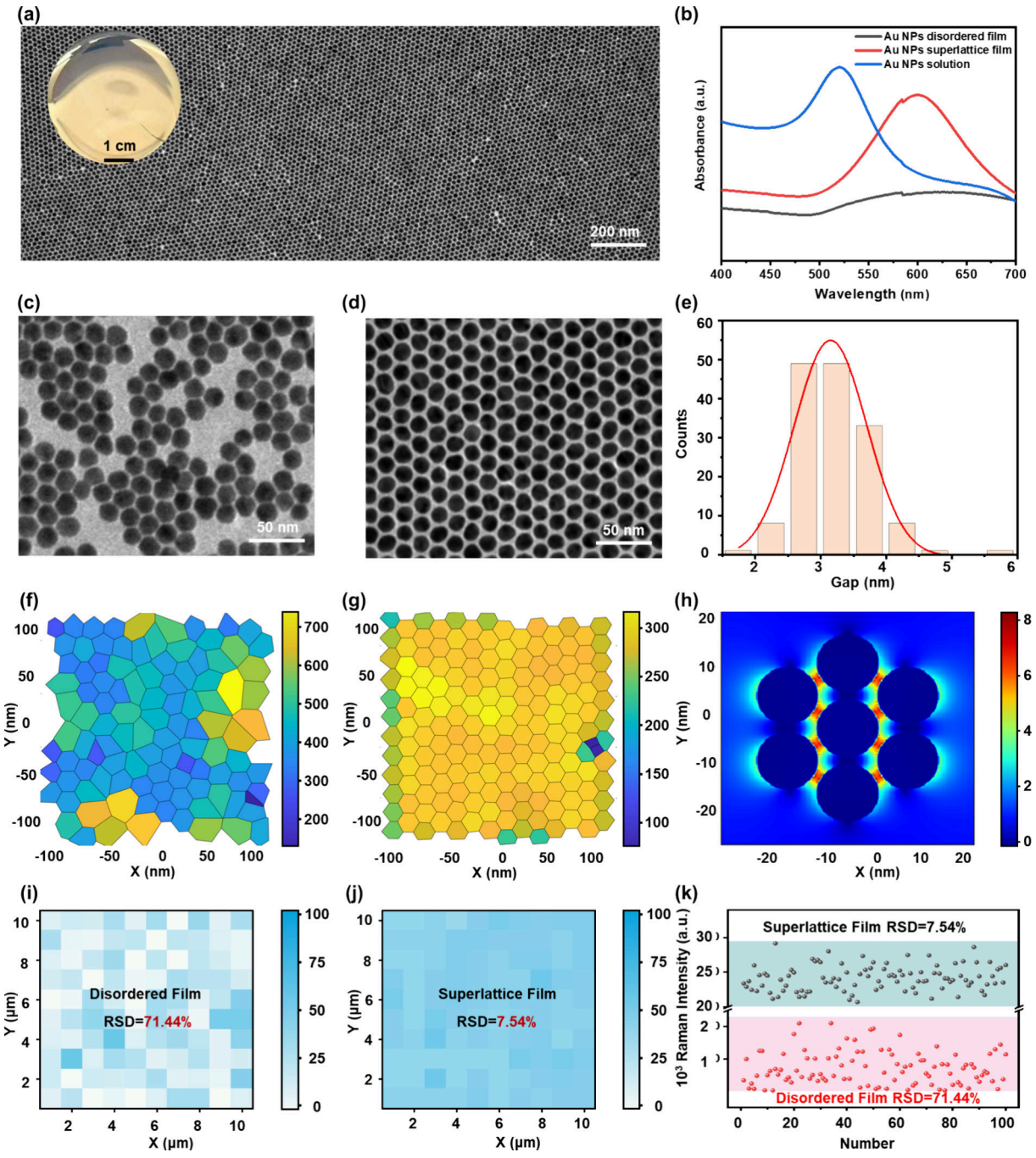

Figure 2. Preparation and characterization of Au NP superlattice substrates. (a) Macroscopic representation of the superlattice film and transmission electron microscopy (TEM) image. (b) UV−vis spectra of the Au NP solution, disordered film, and superlattice film. (c) TEM images of the Au NP disordered film. (d) TEM image of the Au NP superlattice film. (e) Statistical analysis of interparticle spacing in the Au NP superlattice film. (f) Voronoi diagram of the Au NP disordered film. (g) Voronoi diagram of the Au NP superlattice film. (h) FDTD simulation of the Au NP superlattice film. (i) Raman mappings over a 10 μm × 10 μm region of the Au NP disordered film. (j) Raman mappings over a 10 μm × 10 μm region of the Au NP superlattice film. (k) Raman signal distribution statistics.

the hollow architecture of the Au@Au−Ag nanocages and revealed a distinct elemental distribution between the core and shell regions (Figures 3d and S13). To further elucidate the "hot spots" enhancement mechanism of Raman within the hollow nanogap, FDTD simulations of electromagnetic field distribution were carried out.[36] As illustrated in Figure 3e−g, the FDTD simulation results revealed a significantly enhanced electric field intensity within the nanogap between the outer Au−Ag alloy shell and the inner Au core compared to other regions, which was consistent with theoretical expectations. This observation indicates that metallic nanostructures under light excitation exhibit localized surface plasmon resonance (LSPR), and that these electromagnetically enhanced nanogaps act as critical hot spots, playing a decisive role in the amplification of SERS signals. As shown in Figure 3h, in a comparative SERS study using 4-MBA as a probe molecule, the double-shelled

https://doi.org/10.1021/acssensors.5c04789
ACS Sens. 2026, 11, 2763−2773

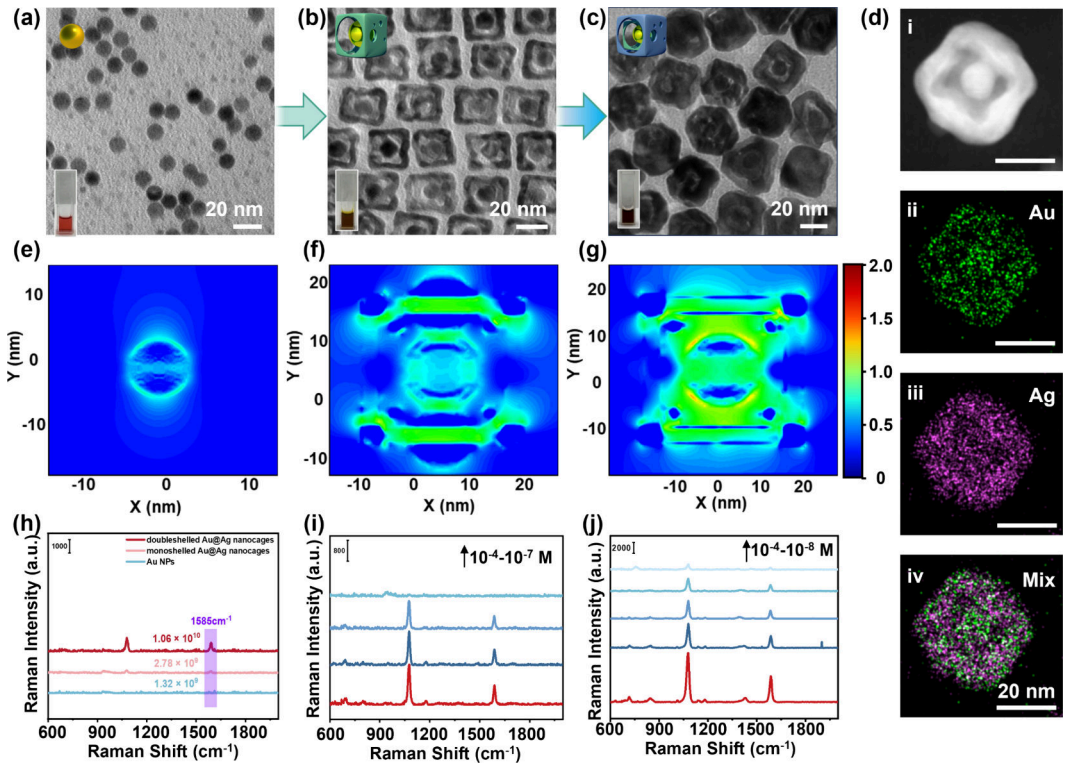

Figure 3. Preparation and characterization of the double-shelled hollow Au@Au−Ag nanocages. TEM image of (a) Au NP seed, (b) mono-shelled hollow Au@Au−Ag nanocages, and (c) double-shelled hollow Au@Au−Ag nanocages. (d) Energy-dispersive X-ray spectra of the double-shelled hollow Au@Au−Ag nanocages. High-angle annular dark-field scanning transmission electron microscope (HAADF-STEM) images and the corresponding elemental mapping showing the spatial distribution of Au (green) and Ag (purple). FDTD simulation of (e) Au NPs, (f) mono-shelled hollow Au@Au−Ag nanocages, and (g) double-shelled hollow Au@Au−Ag nanocages. (h) Comparison of Raman intensity from different nanoparticles deposited on the superlattice substrate. (i) SERS intensity of 4-MBA at gradient concentrations on the Au NP disordered film substrate overlaid with the double-shelled hollow Au@Au−Ag nanocages. (j) SERS intensity of 4-MBA at gradient concentrations on the Au NP superlattice film substrate overlaid with the double-shelled hollow Au@Au−Ag nanocages.

hollow Au@Au−Ag nanocages exhibited significantly superior performance compared to Au NPs. This was evidenced by a pronounced signal enhancement of approximately 2-fold at the characteristic Raman peak located at 1583 cm^{-1}.[37]

Furthermore, the sandwiched superlattice structure of Au NPs demonstrates superior detection capability for 4-MBA, reaching a limit of 10^{-8} M, compared to a sandwiched film of disordered Au NPs (Figure 3i,j). At an analyte concentration of 10^{-7} M, the disordered Au nanoparticle film fails to produce a discernible and reproducible SERS signal, as the sparse and randomly distributed hotspots are insufficient to consistently overcome the instrumental noise floor. This limitation highlights the inherent challenge of achieving reliable ultralow-concentration detection on non-uniform plasmonic substrates (Figure S14). Remarkably, the SERS enhancement factor of this sandwich complex platform was determined to be as high as 1.57×10^{11} (Figure S15 and Note S1).

Enhanced SERS from Sandwiched Au NP Superlattices

Alterations in DA concentration serve as a crucial biochemical indicator for diagnosing and monitoring depression. The following section describes the highly sensitive and stable SERS substrate of our sensing chip, using dopamine as a model analyte, which holds significant promise for application in depression diagnostics. The advanced SERS platform relied on a bifunctional heterostructure design. Its upper layer comprised double-shelled hollow Au@Au−Ag nanocages, chosen for their superior plasmonic properties including strong electromagnetic field enhancement and abundant hotspot generation. The functionalization of these nanocages proceeded in multiple steps: thiol-modified DNA_1 was first conjugated to serve as the recognition element, after which the Raman reporter molecule 5, 5'-dithiobis-(2-nitrobenzoic acid) (DTNB) was bound (Figures 4a-i and S16−18). The disulfide bond in DTNB was cleaved, which allowed the molecule to anchor to the Au surface via an Au−S bond. This process resulted in a characteristic Raman signature from the asymmetric stretching vibration of the nitro group at 1330 cm^{-1}.[38] The underlying substrate was composed of a highly ordered superlattice of monodisperse Au NPs, which was fabricated through a self-assembly process that ensured exceptional spatial uniformity. This superlattice film was further modified with a thiol-modified complementary DNA_2 strand specific to the DA aptamer, which was immobilized via stable Au−S bonds. (Figures 4a-ii and S19). The dense and regular arrangement of Au NPs in the superlattice significantly enhanced the overall SERS activity through efficient plasmonic coupling and near-field amplification. When the two layers were brought into contact, the aptamer on the nanocage and the complementary DNA strand on the Au NPs superlattice hybridized, forming a zipper-like nanodimer architecture (Figure 4a-iii). This hybridization event not only ensured firm integration of the two layers but also induced strong interparticle plasmonic coupling, which dramatically boosted the Raman intensity of DTNB and provided high

https://doi.org/10.1021/acssensors.5c04789
ACS Sens. 2026, 11, 2763−2773

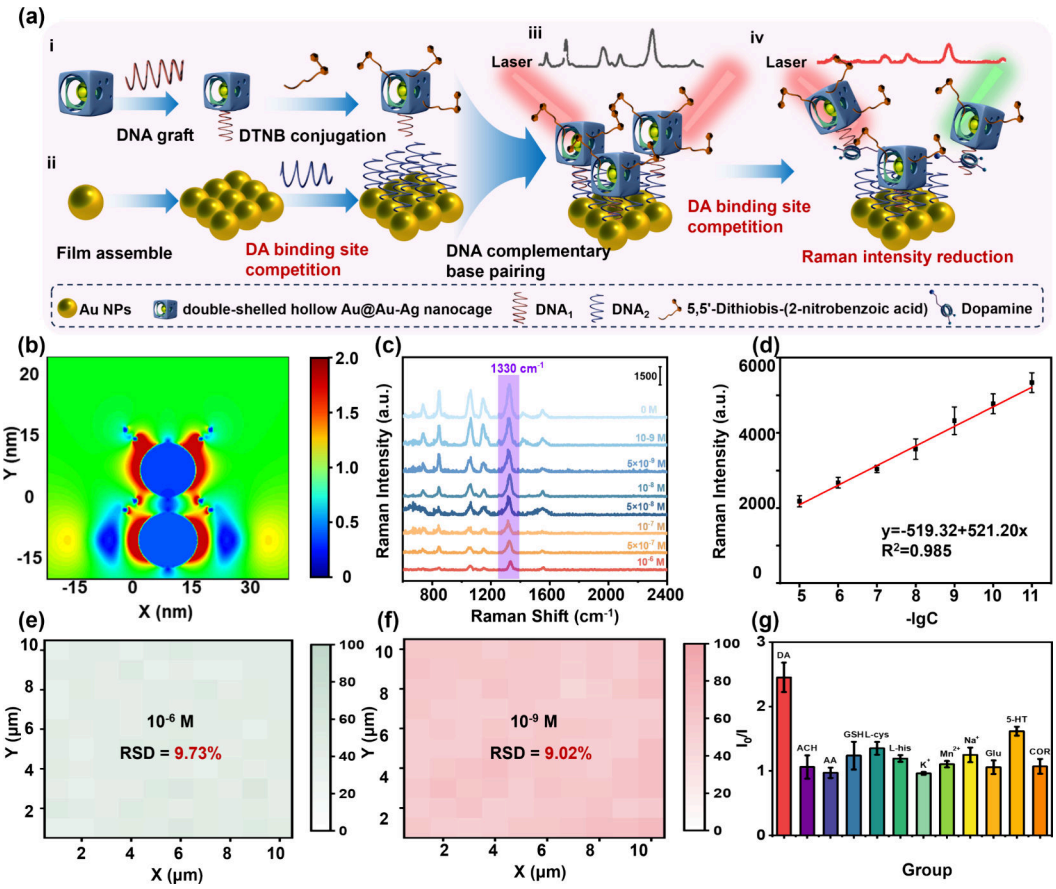

Figure 4. Biosensing performance of the sandwiched Au NP superlattice sensing platform. (a) Schematic diagram of the construction of a double-layer heterogeneous sandwich structure and its dopamine sensing process. (b) Electromagnetic field simulation of the sandwiched Au NP superlattices under laser excitation. (c) Decrease in SERS signal intensity across a concentration range of dopamine that includes physiological dopamine concentration. (d) Calibration curve relating dopamine concentration to SERS peak intensity. (e) Raman mappings of the sensing platform over a 10 μm × 10 μm area at 10^{-6} M dopamine. (f) Raman mappings of the sensing platform over a 10 μm × 10 μm area at 10^{-9} M dopamine. (g) Comparison of SERS responses to various interfering amino acids and ions.

structural stability. The introduction of DA instigated a competitive binding process: owing to the higher affinity between DA and the DNA aptamer (DNA_2) compared to the DNA duplex, free DA molecules displaced the hybridized complementary strand, which resulted in the dissociation of the nanocages from the superlattice substrate (Figure 4a-iv). The displacement event caused a measurable drop in SERS intensity that inversely correlated with the sample's DA concentration. Quantitative tracking of the DTNB peak attenuation thus allowed for highly sensitive and stable DA detection using this SERS substrate. Consequently, the system functioned as a target-specific SERS nanotag, demonstrating both intense signal output and high affinity for DA. Complementary base pairing stabilized the entire architecture and preserved its orderly arrangement. As illustrated in Figure 4b, the FDTD simulation revealed a uniform distribution of hotspots over the bilayer film, which was consistent with theoretical expectations. The enhanced SERS performance arises from a cascaded electromagnetic coupling between the superlattice substrate and the nanocage resonator, in which the near field of the superlattice further polarizes the nanocage, leading to highly confined hotspots within the nanogaps (Figures S20 and 21).[39] Furthermore, the SERS sensitivity and reproducibility of the composite substrate were validated through systematic evaluation. The results showed that the SERS signal intensity for DA depended clearly on its concentration, and signals could be detected even at an ultralow concentration of 1×10^{-9} M (Figure 4c). Using the peak at 1330 cm^{-1} as the characteristic band, a strong linear relationship (R^2 = 0.985) was observed with DA concentration (Figure 4d). Based on the calibration curve equation and the signals from the standard control samples, the limit of detection (LOD) for this platform was determined to be approximately 4.89×10^{-14} M, as measured in deionized water under interference-free conditions. The homogeneity assessment confirmed the excellent uniformity of the SERS signals, showing minimal variation (RSD < 9.73%) at DA concentrations spanning from 10^{-6} M to 10^{-9} M (Figure 4e,f). The high reproducibility was a critical attribute for practical applications because it ensured reliable detection and quantification over a wide dynamic range. To evaluate the detection specificity of the sensor, additional substances including acetylcholine (ACH), glutathione (GSH), AA, *L*-cysteine (*L*-cys), *L*-histidine (*L*-his), and some common metal ions were introduced at a uniform concentration of 0.1 mM. Compared to DA, these non-target analytes produced negligible Raman signals (Figures 4g and S22). This contrast demonstrated the sensor's excellent selectivity for DA. To further simulate real sweat environments, interference tests were performed in mixed solutions containing multiple biomarkers and ions simultaneously. As shown in Figure S23, the dopamine-induced signal-off response remained stable even in

https://doi.org/10.1021/acssensors.5c04789
ACS Sens. 2026, 11, 2763−2773

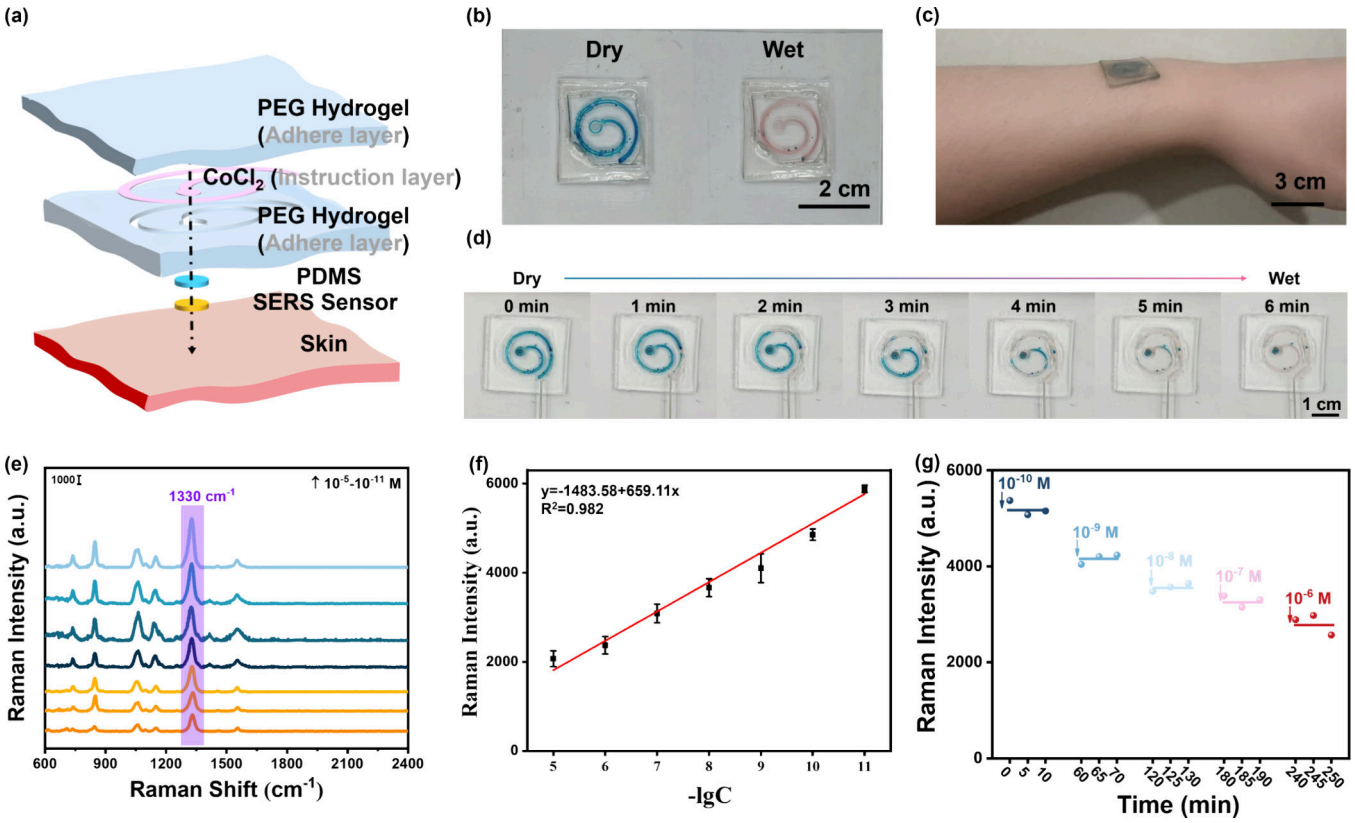

Figure 5. Wearable sweat sensor for non-invasive depression monitoring. (a) Schematic diagram of the structural design and functional components of the SERS sensor. (b) Response of the hydrophilic microchannel to varying water content, demonstrating its moisture-indicating capability. (c) Optical image showing the sensor attached to skin surface, highlighting its flexibility and conformal adhesion. (d) Flowchart of color change in the hydrogel fluid channel over time. (Full color change achieved in 6 min; channel capacity: 120 μL). (e) Detection trend and negative correlation between SERS intensity and dopamine concentration in artificial sweat at standard concentrations. (f) Linear relationship between SERS signal intensity and dopamine concentration. (g) Long-term signal stability and dynamic response of the wearable sensor under progressively increasing dopamine concentrations.

this multi-component system, demonstrating strong resistance to cross-interference. This robustness can be attributed to the DNA-guided competitive displacement mechanism, in which target-specific aptamer recognition governs the release of the SERS nanotags.

Wearable Sweat Sensor for Non-invasive Depression Monitoring

A flexible, wearable SERS sweat sensor patch was fabricated by integrating the sandwiched Au NPs superlattice substrate with a bio-adhesive hydrogel, building upon its outstanding stability and detection capabilities (Figure 5a). This design included microfluidic channels within the hydrogel matrix that played a critical role in sweat sampling; they effectively minimized surface contamination and mitigated evaporation. The sandwiched Au NPs superlattices substrate was fabricated on a PDMS support layer, and securely positioned beneath the microchannel architecture of hydrogel. Capitalizing on the inherent skin-adhesive property of the hydrogel, the sensor achieved conformal contact with the curvilinear skin surface, which ensured both mechanical compliance and enhanced wearer comfort. Beyond serving as a biocompatible adhesive interface, the hydrogel facilitated efficient fluidic transport of sweat through its designed microchannels toward the sensing zone. Additionally, the sensing substrate was securely anchored to the hydrogel through a PDMS interlayer that provided mechanical stability and deformation resistance. This setup allowed sweat to be autonomously drawn through microchannels into an open detection region during on-body monitoring, where it was preconcentrated by evaporation before SERS analysis. Cobalt chloride ($CoCl_2$) was used solely as a hydration-responsive colorimetric indicator to visualize sweat transport in the hydrogel microchannel, and control experiments confirmed that it does not interfere with the SERS detection (Figures 5b and S24). As shown in Figure 5c, a dry sensing chip was adhered to the skin surface, presenting as a dark blue patch. To validate the performance of the sensor, deionized water was introduced at the center and allowed to flow toward the peripheral indicator zone. As shown in Figure 5d, the blue area progressively receded as the pink region expands, with the color transition closely corresponding to the direction of water flow (Table S1). Notably, the observed decrease in SERS intensity with increasing dopamine concentration originates from a competitive displacement mechanism: dopamine binding to the aptamer disrupts the DNA "nanolock", leading to the release of DTNB-labeled nanocages from the superlattice surface and a consequent reduction in SERS hot-spot density. As shown in Figure 5e,f, calibration of dopamine detection in artificial sweat yields a limit of detection of 3.78×10^{-14} M, yielding a strong linear correlation ($R^2 = 0.982$). The effective coverage of typical physiological DA concentrations in human sweat (0−2.5 μM) by the sensor's detection range

https://doi.org/10.1021/acssensors.5c04789
ACS Sens. 2026, 11, 2763−2773

demonstrated its strong potential for practical monitoring of dynamic sweat biomarkers. Figure 5g further demonstrates the real-time dynamic sensing capability of the wearable SERS platform. Upon stepwise increases in dopamine concentration, the SERS signal exhibits rapid and well-defined decreases, with each signal plateau corresponding to a stable response at a given concentration level. Notably, the signal remains stable within each concentration stage without noticeable drift, indicating good temporal stability of the sensing interface. The clear stepwise signal transitions confirm that the sensor can reliably track continuous changes in dopamine concentration over time within a single device, highlighting its suitability for real-time, on-body monitoring applications.

To evaluate the performance of the wearable sensor under realistic, dynamic conditions, longitudinal on-body wear trials were conducted involving 10 healthy adult volunteers (Table S2). The study design incorporated periods of rest and moderate physical activity to induce natural variations in sweat secretion rate and composition. During continuous wearing, the sensor maintained stable conformal contact with the skin and exhibited consistent SERS signal output without noticeable degradation. As shown in Figure S25, the intensity of the characteristic DTNB Raman peak at 1330 cm^{-1} displayed clear temporal evolution, enabling real-time tracking of sweat dopamine fluctuations over extended periods. Notably, the sensor demonstrated stable baseline signals during resting phases and reproducible signal changes upon transition to physical activity, reflecting its ability to respond dynamically to physiologically induced variations in sweat composition. These results confirm that the platform can operate reliably under prolonged, on-body conditions involving sweat generation, evaporation, and compositional changes, highlighting its robustness for wearable sensing applications. To benchmark the performance of the proposed platform, a comparative analysis was conducted against recently reported advanced SERS-based dopamine sensors (Table S3).[40−46] As summarized, the present work achieves an ultralow detection limit while uniquely combining high electromagnetic enhancement with a fully integrated wearable configuration. Notably, unlike many reported systems evaluated in standard solutions, our platform is validated in sweat-relevant conditions with on-body-compatible integration, highlighting its practical advantages for wearable sensing applications.

CONCLUSIONS

This study develops a wearable sweat sensor that integrates a sandwiched Au NPs superlattice into an adhesive hydrogel patch for non-invasive dopamine monitoring, a key depression biomarker. The patch shows superior sensitivity, stability, and practicality, positioning it as a promising tool for mental health diagnostics. Its heterostructure merges a bottom layer of closely-packed Au NPs superlattice with a top layer of functionalized double-shelled hollow Au@Au−Ag nanocages, generating dense, uniform plasmonic hotspots. This design produces strong electromagnetic enhancement, resulting in a high enhancement factor of 1.57×10^{11} and excellent signal reproducibility (RSD = 9.02%) over a wide range. The sensor detects dopamine with nanomole sensitivity (3.78×10^{-14} M), exhibits a wide linear response, and maintains high specificity against interferents. A biocompatible hydrogel enables conformal skin contact, efficient microfluidic sweat uptake, and comfortable long-term wear. The hydrogel's inherent adhesion, transparency, and dehydration resistance further ensure monitoring stability. A built-in visual flow indicator also provides user-friendly operation and real-time feedback. Collectively, this work provides a robust and scalable platform for continuous, non-invasive biomarker tracking, underscoring the promise of SERS-based wearables in personalized depression care and precision medicine.

ASSOCIATED CONTENT

Data Availability Statement

The data that support the findings of this study are available in the supplementary material of this article.

Supporting Information

The Supporting Information is available free of charge at https://pubs.acs.org/doi/10.1021/acssensors.5c04789.

Detailed experimental and characterization data, including materials synthesis and fabrication procedures for hydrogels and plasmonic nanostructures; physicochemical, mechanical, optical, and biocompatibility characterizations; morphological and compositional analyses by TEM, SEM, EDS, and UV−vis-NIR spectroscopy; FDTD simulations of electromagnetic field enhancement; SERS performance evaluation and enhancement factor calculations; dopamine sensing performance, selectivity, and anti-interference studies in artificial and human sweat; dynamic sweat-monitoring results from human volunteers; and a comparative summary of recently reported SERS-based dopamine sensors (DOCX)

AUTHOR INFORMATION

Corresponding Authors

Shuangshuang Wu − *Key Laboratory of Organosilicon Chemistry and Material Technology, Ministry of Education, Zhejiang Key Laboratory of Organosilicon Material Technology, College of Material, Chemistry and Chemical Engineering, Department of Orthopedics, Hangzhou Normal University Affiliated Hospital, Hangzhou Normal University, Zhejiang, Hangzhou 311121, P. R. China;* Email: wuss@hznu.edu.cn

Liping Song − *Key Laboratory of Organosilicon Chemistry and Material Technology, Ministry of Education, Zhejiang Key Laboratory of Organosilicon Material Technology, College of Material, Chemistry and Chemical Engineering, Department of Orthopedics, Hangzhou Normal University Affiliated Hospital, Hangzhou Normal University, Zhejiang, Hangzhou 311121, P. R. China;* Email: slp@hznu.edu.cn

Youju Huang − *Key Laboratory of Organosilicon Chemistry and Material Technology, Ministry of Education, Zhejiang Key Laboratory of Organosilicon Material Technology, College of Material, Chemistry and Chemical Engineering, Department of Orthopedics, Hangzhou Normal University Affiliated Hospital, Hangzhou Normal University, Zhejiang, Hangzhou 311121, P. R. China;* orcid.org/0000-0001-5815-9784; Email: huangyouju@hznu.edu.cn

Authors

Hangzhe Shao − *Key Laboratory of Organosilicon Chemistry and Material Technology, Ministry of Education, Zhejiang Key Laboratory of Organosilicon Material Technology, College of Material, Chemistry and Chemical Engineering, Department of*

https://doi.org/10.1021/acssensors.5c04789
ACS Sens. 2026, 11, 2763−2773

Orthopedics, Hangzhou Normal University Affiliated Hospital, Hangzhou Normal University, Zhejiang, Hangzhou 311121, P. R. China

Lingli Zhang – *Key Laboratory of Organosilicon Chemistry and Material Technology, Ministry of Education, Zhejiang Key Laboratory of Organosilicon Material Technology, College of Material, Chemistry and Chemical Engineering, Department of Orthopedics, Hangzhou Normal University Affiliated Hospital, Hangzhou Normal University, Zhejiang, Hangzhou 311121, P. R. China*

Bohang Ye – *Key Laboratory of Organosilicon Chemistry and Material Technology, Ministry of Education, Zhejiang Key Laboratory of Organosilicon Material Technology, College of Material, Chemistry and Chemical Engineering, Department of Orthopedics, Hangzhou Normal University Affiliated Hospital, Hangzhou Normal University, Zhejiang, Hangzhou 311121, P. R. China*

Qiaoyun Luo – *Key Laboratory of Organosilicon Chemistry and Material Technology, Ministry of Education, Zhejiang Key Laboratory of Organosilicon Material Technology, College of Material, Chemistry and Chemical Engineering, Department of Orthopedics, Hangzhou Normal University Affiliated Hospital, Hangzhou Normal University, Zhejiang, Hangzhou 311121, P. R. China*

Kanzhen Tong – *Key Laboratory of Organosilicon Chemistry and Material Technology, Ministry of Education, Zhejiang Key Laboratory of Organosilicon Material Technology, College of Material, Chemistry and Chemical Engineering, Department of Orthopedics, Hangzhou Normal University Affiliated Hospital, Hangzhou Normal University, Zhejiang, Hangzhou 311121, P. R. China*

Complete contact information is available at: https://pubs.acs.org/doi/10.1021/acssensors.5c04789

Author Contributions

[#]H.S. and S.W. contributed equally to this work. H.S., S.W., L.S., and Y.H. conceived the concept and designed the experiments. H.S. and L.S. conducted the sandwich-structured superlattice and performed the optical measurements with the help of L.Z., B.Y., and Q.L. H.S., S.W., and K.T. conducted the skin-conformal sandwich-structured platform. H.S., S.W., and Y.H. analyzed the data and wrote the manuscript together with discussion with all authors.

Ethics Statement

The experiments involving human subjects have been performed with the full, informed consent of the volunteers.

Notes

The authors declare no competing financial interest.

■ ACKNOWLEDGMENTS

This work was financially supported in part by the "Pioneer" and "Leading Goose" R&D Program of Zhejiang (No. 2025C02250(SD2)), the National Natural Science Foundation of China (Nos. U25A20385, 22304042, 52222316, and 52573293), the Zhejiang Provincial Natural Science Foundation of China (No. LZ22B050001), the Start-up Funding from Hangzhou Normal University (Nos. 4095C50223204052 and 4095C5022421510), the China Postdoctoral Science Foundation (No. 2024M763695), and the "Pioneer" and "Leading Goose" R&D Program of Zhejiang (No. 2024C03195).

■ REFERENCES

(1) Wang, T.; Wang, M.; Wang, J.; Yang, L.; Ren, X.; Song, G.; Chen, S.; Yuan, Y.; Liu, R.; Pan, L.; Li, Z.; Leow, W. R.; Luo, Y.; Ji, S.; Cui, Z.; He, K.; Zhang, F.; Lv, F.; Tian, Y.; Cai, K.; Yang, B.; Niu, J.; Zou, H.; Liu, S.; Xu, G.; Fan, X.; Hu, B.; Loh, X. J.; Wang, L.; Chen, X. A chemically mediated artificial neuron. *Nat. Electron.* **2022**, *5* (9), 586–595.

(2) Li, Z.; Lu, J.; Ji, T.; Xue, Y.; Zhao, L.; Zhao, K.; Jia, B.; Wang, B.; Wang, J.; Zhang, S.; Jiang, Z. Self-Healing Hydrogel Bioelectronics. *Adv. Mater.* **2024**, *36* (21), No. 2306350.

(3) Das, P.; Marvi, P. K.; Ganguly, S.; Tang, X.; Wang, B.; Srinivasan, S.; Rajabzadeh, A. R.; Rosenkranz, A. MXene-Based Elastomer Mimetic Stretchable Sensors: Design, Properties, and Applications. *Nano-Micro Lett.* **2024**, *16* (1), 135.

(4) Roy, A.; Afshari, R.; Jain, S.; Zheng, Y.; Lin, M.-H.; Zenkar, S.; Yin, J.; Chen, J.; Peppas, N. A.; Annabi, N. Advances in conducting nanocomposite hydrogels for wearable biomonitoring. *Chem. Soc. Rev.* **2025**, *54* (5), 2595–2652.

(5) Nandam, L. S.; Brazel, M.; Zhou, M.; Jhaveri, D. J. Cortisol and Major Depressive Disorder-Translating Findings from Humans to Animal Models and Back. *Front. Psychiatry* **2020**, *10*, 974.

(6) Moncrieff, J.; Cooper, R. E.; Stockmann, T.; Amendola, S.; Hengartner, M. P.; Horowitz, M. A. The serotonin theory of depression: a systematic umbrella review of the evidence. *Mol. Psychiatry* **2022**, *28* (8), 3243–3256.

(7) Wang, T.; Liu, T.; Zhu, X.; Zhang, M.; Jiang, J.; Zhang, Z.; Huang, Y.; Wang, Y. High-entropy Prussian blue analogues-mediated flexible field-effect transistor for wearable sweat dopamine monitoring. *Biosens. Bioelectron.* **2025**, *289*, No. 117889.

(8) Baik, J.-H. Stress and the dopaminergic reward system. *Exp. Mol. Med.* **2020**, *52* (12), 1879–1890.

(9) Tamura, T.; Sugihara, G.; Okita, K.; Mukai, Y.; Matsuda, H.; Shiwaku, H.; Takagi, S.; Daisaki, H.; Tateishi, U.; Takahashi, H. Dopamine dysfunction in depression: application of texture analysis to dopamine transporter single-photon emission computed tomography imaging. *Transl. Psychiatry* **2022**, *12* (1), 309.

(10) Mahato, K.; Saha, T.; Ding, S.; Sandhu, S. S.; Chang, A.-Y.; Wang, J. Hybrid multimodal wearable sensors for comprehensive health monitoring. *Nat. Electron.* **2024**, *7* (9), 735–750.

(11) Wu, S.; Liu, S.; Li, T.; Li, J.; Wang, L.; Wang, T. Molecular intelligent perception on soft interfaces. *Sci. Bull.* **2024**, *69* (5), 578–582.

(12) Ye, C.; Lukas, H.; Wang, M.; Lee, Y.; Gao, W. Nucleic acid-based wearable and implantable electrochemical sensors. *Chem. Soc. Rev.* **2024**, *53* (15), 7960–7982.

(13) Min, J.; Tu, J.; Xu, C.; Lukas, H.; Shin, S.; Yang, Y.; Solomon, S. A.; Mukasa, D.; Gao, W. Skin-Interfaced Wearable Sweat Sensors for Precision Medicine. *Chem. Rev.* **2023**, *123* (8), 5049–5138.

(14) Davis, N.; Heikenfeld, J.; Milla, C.; Javey, A. The challenges and promise of sweat sensing. *Nat. Biotechnol.* **2024**, *42* (6), 860–871.

(15) Huang, C.; Yang, W.; Wang, H.; Huang, S.; Gao, S.; Li, D.; Liu, J.; Hou, S.; Feng, W.; Wang, Z.; Li, F.; Hao, Z.; Zhao, X.; Hu, P.; Pan, Y. Flexible/Regenerative Nanosensor with Automatic Sweat Collection for Cytokine Storm Biomarker Detection. *ACS Nano* **2024**, *18* (32), 21198–21210.

(16) Yao, S.; Ren, P.; Song, R.; Liu, Y.; Huang, Q.; Dong, J.; O'Connor, B. T.; Zhu, Y. Nanomaterial-Enabled Flexible and Stretchable Sensing Systems: Processing, Integration, and Applications. *Adv. Mater.* **2019**, *32* (15), No. 1902343.

(17) Sempionatto, J. R.; Lasalde-Ramírez, J. A.; Mahato, K.; Wang, J.; Gao, W. Wearable chemical sensors for biomarker discovery in the omics era. *Nat. Rev. Chem.* **2022**, *6* (12), 899–915.

(18) Chen, X.; Wang, C.; Wei, W.; Liu, Y.; Ge, S. S.; Zhou, L.; Kong, H. Flexible and sensitive pressure sensor with enhanced

breathability for advanced wearable health monitoring. *npj Flex. Electron.* **2025**, *9* (1), 101.
(19) Yang, X.; Yi, J.; Wang, T.; Feng, Y.; Wang, J.; Yu, J.; Zhang, F.; Jiang, Z.; Lv, Z.; Li, H.; Huang, T.; Si, D.; Wang, X.; Cao, R.; Chen, X. Wet-Adhesive On-Skin Sensors Based on Metal–Organic Frameworks for Wireless Monitoring of Metabolites in Sweat. *Adv. Mater.* **2022**, *34* (44), No. 2201768.
(20) Wei, Z.; Jia, L.; Yu, J.; Xu, H.; Guo, X.; Xiang, T.; Zhou, S. Environmentally tolerant multifunctional eutectogel for highly sensitive wearable sensors. *Mater. Horiz.* **2025**, *12* (8), 2604–2618.
(21) Chen, S.; Qiao, Z.; Niu, Y.; Yeo, J. C.; Liu, Y.; Qi, J.; Fan, S.; Liu, X.; Lee, J. Y.; Lim, C. T. Wearable flexible microfluidic sensing technologies. *Nat. Rev. Bioeng.* **2023**, *1* (12), 950–971.
(22) Matzeu, G.; Mogas-Soldevila, L.; Li, W.; Naidu, A.; Turner, T. H.; Gu, R.; Blumeris, P. R.; Song, P.; Pascal, D. G.; Guidetti, G.; Li, M.; Omenetto, F. G. Large-Scale Patterning of Reactive Surfaces for Wearable and Environmentally Deployable Sensors. *Adv. Mater.* **2020**, *32* (28), No. 2001258.
(23) Gao, F.; Liu, C.; Zhang, L.; Liu, T.; Wang, Z.; Song, Z.; Cai, H.; Fang, Z.; Chen, J.; Wang, J.; Han, M.; Wang, J.; Lin, K.; Wang, R.; Li, M.; Mei, Q.; Ma, X.; Liang, S.; Gou, G.; Xue, N. Wearable and flexible electrochemical sensors for sweat analysis: a review. *Microsyst. Nanoeng.* **2023**, *9* (1), 1.
(24) Fan, W.; Lei, R.; Dou, H.; Wu, Z.; Lu, L.; Wang, S.; Liu, X.; Chen, W.; Rezakazemi, M.; Aminabhavi, T. M.; Li, Y.; Ge, S. Sweat permeable and ultrahigh strength 3D PVDF piezoelectric nanoyarn fabric strain sensor. *Nat Commun.* **2024**, *15* (1), 3509.
(25) Zhang, Z.; Li, K.; Li, Y.; Zhang, Q.; Wang, H.; Hou, C. Dual-Function Wearable Hydrogel Optical Fiber for Monitoring Posture and Sweat pH. *ACS Sens.* **2024**, *9* (6), 3413–3422.
(26) Lau, C. Y.; Duan, H.; Wang, F.; He, C. B.; Low, H. Y.; Yang, J. K. W. Enhanced Ordering in Gold Nanoparticles Self-Assembly through Excess Free Ligands. *Langmuir* **2011**, *27* (7), 3355–3360.
(27) Zhu, K.; Yang, K.; Zhang, Y.; Yang, Z.; Qian, Z.; Li, N.; Li, L.; Jiang, G.; Wang, T.; Zong, S.; Wu, L.; Wang, Z.; Cui, Y. Wearable SERS Sensor Based on Omnidirectional Plasmonic Nanovoids Array with Ultra-High Sensitivity and Stability. *Small* **2022**, *18* (32), No. 2201508.
(28) Moretti, C.; Goldmann, C.; Imperor-Clerc, M.; Abécassis, B. Gold Nanoparticle Superlattices: Conditions for Long-Range Order, Moiré Patterns, and Binary Phase from a Single Population. *Chem. Mater.* **2023**, *35* (17), 6637–6650.
(29) Xiahou, Y.; Liu, J.; Zheng, J.; Yi, J.; Wang, D.; Xia, H. Performance improvement of macroscopical film of gold nanoparticles as temperature sensor derived from its mono-crystallinity. *Chem. Eng. J.* **2023**, *460*, No. 141835.
(30) Li, Y.; Sun, Z.; Chai, S.; Zhang, Z.; Li, Y.; Zhu, C.; Fan, D. Tissue-like Soft Dual-Network Hydrogel Patch with Instant/Tunable Adhesion and Microenvironment Modulation for Infected Wound Healing. *ACS Nano* **2025**, *19* (30), 27714–27730.
(31) Liu, T.; Nong, Z.; Li, Y.; Liu, Z.; Fan, Z.; Liu, H.; Liu, Q.; Qiu, J.; Wang, Q.; Liu, Z. Eutectogel Skin Electrodes with Superior Adhesion, Sweat Resistance, and Long-Term Stability for Electrophysiological Signal Monitoring. *Adv. Funct. Mater.* **2025**, *35* (49), No. e03568.
(32) Song, L.; Zhu, X.; Yang, J.; Li, X.; Yu, Y.; Liu, Y.; Huang, L.; Jiang, S.; Huang, Y. Superfast and Wafer-Scale Superlattice Film Engineering Enabled by an Ultralow-Interfacial-Energy Microenvironment. *J.Am.Chem.Soc.* **2025**, *147* (12), 10369–10381.
(33) Zhu, A.; Ali, S.; Xu, Y.; Ouyang, Q.; Chen, Q. A SERS aptasensor based on Au NPs functionalized PDMS film for selective and sensitive detection of Staphylococcus aureus. *Biosens. Bioelectron.* **2021**, *172*, No. 112806.
(34) Ye, H.; Chen, X.; Huang, X.; Li, C.; Yin, X.; Zhao, W.; Wang, T. Patterned Gold Nanoparticle Superlattice Film for Wearable Sweat Sensors. *Nano Lett.* **2024**, *24* (35), 11082–11089.
(35) Fu, Q.; Zhou, J.; Wang, X.; Xu, W.; Chen, X.; Chen, L.; Huang, Y. Nanoscale Engineering of 3D Intragaps and Compositions in Multimetallic Hollow Superstructures for Enhanced Catalysis. *Nano Lett.* **2025**, *25* (12), 4696–4704.
(36) Estévez-Varela, C.; Núñez-Sánchez, S.; Piñeiro-Varela, P.; Aberasturi, D. J.; deLiz-Marzán, L. M.; Pérez-Juste, J.; Pastoriza-Santos, I. Plexcitonic Nanorattles as Highly Efficient SERS-Encoded Tags. *Small* **2023**, *20* (39), No. 2306045.
(37) Jiang, L.; Wang, X.; Zhou, J.; Fu, Q.; Lv, B.; Sun, Y.; Song, L.; Huang, Y. Plasmonic Multi-Layered Built-in Hotspots Nanogaps for Effectively Activating Analytes. *Adv. Sci.* **2023**, *11* (7), No. 2306125.
(38) Tan, H.-S.; Wang, T.; Han, J.-M.; Liu, M.; Li, S.-S. Dual-signal SERS biosensor based on spindle-shaped gold array for sensitive and accurate detection of miRNA 21. *Sens. Actuators, B* **2024**, *403*, No. 135157.
(39) Langer, J.; Jimenez de Aberasturi, D.; Aizpurua, J.; Alvarez-Puebla, R. A.; Auguié, B.; Baumberg, J. J.; Bazan, G. C.; Bell, S. E. J.; Boisen, A.; Brolo, A. G.; Choo, J.; Cialla-May, D.; Deckert, V.; Fabris, L.; Faulds, K.; García de Abajo, F. J.; Goodacre, R.; Graham, D.; Haes, A. J.; Haynes, C. L.; Huck, C.; Itoh, T.; Käll, M.; Kneipp, J.; Kotov, N. A.; Kuang, H.; Le Ru, E. C.; Lee, H. K.; Li, J.-F.; Ling, X. Y.; Maier, S. A.; Mayerhöfer, T.; Moskovits, M.; Murakoshi, K.; Nam, J.-M.; Nie, S.; Ozaki, Y.; Pastoriza-Santos, I.; Perez-Juste, J.; Popp, J.; Pucci, A.; Reich, S.; Ren, B.; Schatz, G. C.; Shegai, T.; Schlücker, S.; Tay, L.-L.; Thomas, K. G.; Tian, Z.-Q.; Van Duyne, R. P.; Vo-Dinh, T.; Wang, Y.; Willets, K. A.; Xu, C.; Xu, H.; Xu, Y.; Yamamoto, Y. S.; Zhao, B.; Liz-Marzán, L. M. Present and Future of Surface-Enhanced Raman Scattering. *ACS Nano* **2019**, *14* (1), 28–117.
(40) Gwon, Y.; Kim, J.-H.; Lee, S.-W. Quantification of Plasma Dopamine in Depressed Patients Using Silver-Enriched Silicon Nanowires as SERS-Active Substrates. *ACS Sens.* **2024**, *9* (2), 870–882.
(41) Zhang, H.; Wang, R.; Sikdar, D.; Wu, L.; Sun, J.; Gu, N.; Chen, Y. Plasmonic Superlattice Membranes Based on Bimetallic Nano-Sea Urchins as High-Performance Label-Free Surface-Enhanced Raman Spectroscopy Platforms. *ACS Sens.* **2022**, *7* (2), 622–631.
(42) Kim, M.; Choi, Y. S.; Jeong, D. H. SERS detection of dopamine using metal-chelated Ag nanoshell. *RSC Adv.* **2024**, *14* (20), 14214–14220.
(43) Deng, W.; Yuan, L.; Wan, P.; Sun, J.; Kan, C.; Shi, D.; Xu, C.; Lu, J. Piezoelectric-enhanced ultrasensitive ZnO/Ag microcavity SERS substrate for dopamine detection. *Nano Energy* **2025**, *133*, No. 110449.
(44) Guselnikova, O.; Postnikov, P.; Trelin, A.; Švorčík, V.; Lyutakov, O. Dual Mode Chip Enantioselective Express Discrimination of Chiral Amines via Wettability-Based Mobile Application and Portable Surface-Enhanced Raman Spectroscopy Measurements. *ACS Sens.* **2019**, *4* (4), 1032–1039.
(45) Chen, M.; Liu, Z.; Su, B.; Hu, R.; Fu, F.; Jiang, X.; Lin, Z.; Dong, Y. High-Performance Hydrogel SERS Chips with Tunable Localized Surface Plasmon Resonance for Coordinated Electromagnetic Enhancement with Chemical Enhancement. *Adv. Opt. Mater.* **2023**, *11* (7), No. 2202852.
(46) Wang, X.; Shen, S.; Sun, N.; Zhu, Y.; Zhang, J. Neural Network-Assisted Dual-Functional Hydrogel-Based Microfluidic SERS Sensing for Divisional Recognition of Multimolecule Fingerprint. *ACS Sens.* **2025**, *10* (2), 1197–1205.

https://doi.org/10.1021/acssensors.5c04789
ACS Sens. 2026, 11, 2763–2773